

A simplified mechanism for anisotropic constriction in *Drosophila* mesoderm.

Konstantin Doubrovinski^{*,1}, Joel Tchoufag³, and Kranthi Mandadapu^{2,3}

¹Green Center for Systems Biology, University of Texas Southwestern Medical Center, Dallas, TX 75390-9050.

²Chemical Sciences Division, Lawrence Berkeley National Laboratory, Berkeley, United States.

³Department of Chemical and Biomolecular Engineering, University of California, Berkeley, Berkeley, United States.

1 Summary

Understanding how forces and material properties give rise to tissue shapes is a fundamental question in developmental biology. Although *Drosophila* gastrulation is a major system for investigating tissue morphogenesis, there does not exist a consensus mechanical model that explains all the key features of this process. One key feature of *Drosophila* gastrulation is its anisotropy - the mesoderm constricts much more along one axis than along the other. Previous explanations have involved graded stress, anisotropic stresses or material properties, or mechanosensitive feedback. Here we show that these mechanisms are not required to explain the anisotropy of constriction. Instead, constriction can be anisotropic if only two conditions are met: the tissue is elastic, as was demonstrated in our recent study, and the contractile domain is asymmetric. This conclusion is general and does not depend on the

*Correspondence to Konstantin.Doubrovinski@UTSouthwestern.edu

values of model parameters. This model can explain classical tissue grafting experiments and more recent laser ablation studies. Furthermore, this model may provide alternative explanations for experiments in other developmental systems, including *C. elegans* and zebrafish.

2 Introduction

A fundamental process in animal development is gastrulation, whereby a single epithelial sheet gives rise to a multilayered structure (Sweeton et al. 1991; Leptin and Grunewald 1990). In *Drosophila*, gastrulation initiates when the prospective mesoderm cells, which are located in a rectangular domain in the ventral part of the embryo, constrict apically (i.e. on the outer surface of the embryo, see schematic in Figure 1). As the mesodermal cells constrict across their apical faces, they become wedge-shaped and elongate along the apico-basal axis (Sweeton et al. 1991; Leptin and Grunewald 1990). Apical constriction of the mesodermal cells is widely believed to be driven by myosin-generated active stresses in the apical domains of those cells (Dawes-Hoang et al. 2005). In accordance with this, the concentration of apically localized myosin increases dramatically in the constricting cells concomitantly with the onset of apical constriction (Martin et al. 2010). Following apical constriction, the surface of the embryo forms a furrow at the ventral midline. The furrow deepens and closes off; in this way, the mesoderm is brought into the interior of the embryo.

The focus of this study is the initial phase of gastrulation when mesodermal cells constrict apically, before the surface begins to fold inward. Notably, as mesodermal cells shrink, the rectangular mesodermal domain contracts strongly along its shorter axis and much less so along the longer axis. For brevity, the length of the mesodermal domain along the shorter mediolateral axis will be referred to as the “width”, and the length of its longer antero-posterior axis will be referred to as the “length”. Thus, the length to width ratio increases drastically in the course of the constriction of the mesoderm, see schematic in Figure 1. Because mesoderm constriction in *Drosophila melanogaster* is not accompanied by appreciable cell rearrangements, the length to width ratio of individual mesodermal cells must increase in the course of tissue contraction (Martin et al. 2010; Spahn and Reuter 2013).

This anisotropic constriction has been the subject of considerable interest. One key experiment was done in a classical paper by Maria Leptin and

Siegfried Roth (Leptin and Roth 1994). There, patches of mesodermal tissue (either nuclei or cytoplasm) were transplanted into mutant embryos that lacked mesoderm. If the contractile domain were symmetric (e.g. round or square) it would constrict symmetrically, while if the contractile domain were elongated, it would constrict anisotropically. Furthermore, the geometry of contraction of mesodermal patches was independent of the position and orientation of those patches within the embryo and was only dependent on the geometry of the patch. This showed that anisotropic constriction is a locally autonomous effect, and is not for example induced by maternal gradients (i.e. factors that localize in a patterned manner in a freshly laid egg, notably bicoid, nanos, torsolike and dorsal). The mechanism driving anisotropic constriction remained unclear, however. Two more recent papers proposed graded tension (Spahn and Reuter 2013) or mechanosensitivity (in particular, feedback between stress and nematic order of actin filaments, Chanet et al. 2017) as the source of anisotropy. Here, we propose a simple mechanistic explanation for anisotropic constriction of the mesoderm that does not invoke any of these effects.

3 Results

3.1 The model

We start by describing model assumptions, then present the corresponding equations below. We model the surface of the embryo as a flat (two-dimensional) elastic sheet. This elastic sheet may be pictured as a network of spheres connected by springs as shown in Figure 1. The model sheet will contain a rectangular contractile domain with horizontal and vertical dimensions L_x (length) and L_y (width) respectively (see Figure 1). The size of the contractile domain is taken to be much smaller than the size of the simulated sheet in order to avoid boundary effects. In order for this contractile domain to shrink it must carry active contractile stress, or “tension”, which is measured in units of force per unit length. In Figure 1, the presence of active stress in the contractile domain is illustrated by red arrows, which are directed in parallel with the springs. It is assumed that the active stress within the contractile domain is uniform (having the same magnitude everywhere) and isotropic (same magnitude in every direction). In particular, in Figure 1, all motors are the same regardless of the orientation of the correspond-

ing spring or the position of the spring. Outside of the contractile domain the actively-generated stress is absent. In the real embryo, active contractile stress is generated by active myosin motors. Since active contractile stresses do not depend on instantaneous displacement, there is no feedback to force generation in this model.

The above assumptions make up a complete description of the model. Combining these assumptions with standard equations of linear elasticity, assuming that the elastic sheet is in mechanical equilibrium (see (Landau and Lifshitz 1970), in particular Equation 13.4 therein), we have:

$$\frac{E}{2(1+\sigma)}\nabla^2\mathbf{u} + \frac{E}{2(1-\sigma)}\nabla\nabla\cdot\mathbf{u} + \nabla\cdot\boldsymbol{\mu} = 0 \quad , \quad (1)$$

where \mathbf{u} is the in-plane deformation of the sheet, E is Young's modulus (more accurately, this quantity represents Eh , where E is the three-dimensional Young's modulus, and h is the thickness of the sheet), σ is the Poisson's ratio, and $\boldsymbol{\mu}$ is the active stress tensor within the contractile mesodermal domain (and does not, in general, correspond to a conservative force, see e.g. Jülicher et al. 2007). We take active stress to be isotropic, $\boldsymbol{\mu} = \phi\mathbf{I}$, with \mathbf{I} being the identity matrix, and $\phi(\mathbf{r}) = \phi_0\Pi(x/L_x)\Pi(y/L_y)$, where Π denotes the “top hat” function that equals identity between -0.5 and 0.5 and zero otherwise. The magnitude of active stress is constant in the mesodermal domain and zero outside. (If some uniform active stress is present outside the contractile domain, ϕ_0 may be considered the difference between the active stress inside and that outside. Since Equation 1 takes a derivative of stress, the solution depends only on the difference in contractility between the domains.) Note that we ignore viscous relaxation of stresses since it was found experimentally that those stresses persist on a time-scale comparable with (not significantly shorter than) the time-scale of tissue dynamics (Dobrovinski et al. 2017). Finally, we note that the assumption that the elastic sheet is in mechanical equilibrium is an idealization: it is not known whether developmental dynamics proceed adiabatically.

The model is schematically illustrated in Figure 1. The elastic sheet is represented by a spring network with nodes illustrated as spherical beads. Note that for simplicity the illustration was made somewhat misleading: a network of squares is not isotropic, whereas Equation (1) describes an isotropic elastic material. Note that direct rheological measurements have demonstrated that the membrane surface of embryonic tissue is highly elastic and that elasticity persists on a time-scale that is well comparable to the time-scale

of gastrulation (Dobrovinski et al. 2017). Myosin-generated tension in the mesodermal domain is well established (Dawes-Hoang et al. 2005; Martin et al. 2009; Martin et al. 2010).

Additionally, the proposed model involves only a few dimensional parameters. The elastic sheet that represents the epithelium has Young's modulus E which determines the force required to stretch material a given amount and may be thought of as a multi-dimensional counterpart of a spring constant. An elastic material is further characterized by its Poisson's ratio σ , which determines how much a material shrinks in one direction when it is being stretched along a perpendicular direction. Finally, the active stress (or, equivalently, tension) inside the contractile domain has magnitude ϕ_0 . Since tension is assumed to not vary with either space or direction within the contractile domain, only one number is needed to describe this active stress.

3.2 Analysis of the model: constriction geometry

To analyze the behavior of the minimal model (1) we performed numerical simulations; implementation details are given in Appendix A. If the contractile domain is chosen to be asymmetric (i.e. $L_x \gg L_y$, or length larger than width), simulations reveal constriction to be greater along the shorter axis of the domain, see Figure 2a,b,c, and Figure S1. In contrast, when the contractile domain is chosen to be symmetric (i.e. $L_x = L_y$), constriction is equal along both axes, Figure 2f. Thus, this simple model, which involves only elastic material and an isotropic contractile force, replicates the key experimental finding that the anisotropy versus isotropy of constriction is dependent on geometry (Leptin and Roth 1994).

To examine the influence of model parameters on these predictions we performed a parameter sweep (Figure 2d,e). The non-dimensionalized version of Equation 1 has the following dimensionless parameters: the ratio of Young's modulus to active stress magnitude E/ϕ_0 , Poisson's ratio σ , and the length to width ratio of the contractile domain L_x/L_y . The value of Poisson's ratio σ was varied over the whole physically relevant range, which is between 0 and 1/2 (Greaves et al. 2011). It is seen that the qualitative nature of the solution does not vary appreciably with the value of the Poisson's ratio. Simulation results for three different choices of the active stress to stiffness ratio ϕ_0/E are given in Figure 2d. Note that since equation 1 is linear, the displacement is proportional to active stress and therefore the solutions (i.e. the u_x and u_y components of the displacement, shown for one particular

choice of parameters in Figure 2c) for different ϕ_0/E are related by simple scaling. From this it easily follows that anisotropy is zero in the limit of zero force and increases arbitrarily for sufficiently high values of ϕ_0/E . Additionally we systematically examined the influence of the initial aspect ratio of the contractile domain on the final equilibrium geometry (Figure 2e); to this end, we used analytical expressions given in the appendix. It was found that contraction is always asymmetric although the degree of the asymmetry may vary. Symmetric domains contract symmetrically (Figure 2e). In summary, our results are not sensitive to the choice of the elasticity parameters.

To examine the influence of the domain in which the contractile domain is embedded, we performed additional simulations. To this end we simulated square as well as rectangular contractile domains embedded in either square or rectangular stress-free domains. The deformation of the contractile domain becomes essentially independent of the geometry of the embedding domain provided the embedding domain was chosen to be sufficiently large, Figure S2c. To further formally examine the influence of the geometry of the embedding domain, we systematically determined the final equilibrium aspect ratio of the contractile domain as a function of model parameters and the size of the embedding domain. Figure S3 shows that for a fixed geometry of the contractile domain and fixed model parameters, the equilibrium ratio converges to a limit as the embedding domain is made larger and larger. Finally, to further study the influence of the boundary conditions, we compared simulations with both free and fixed boundaries using finite element simulations (Figure S2b). Our results indicate close quantitative agreement in this case as well, again confirming that the boundary effects are irrelevant as long as the embedding domain is chosen to be sufficiently large. Note that since convergence with respect to the size of the embedding domain is reached for very modest sizes of the embedding domain (for the relevant aspect ratio of the contractile domain, see Figure S3), we believe that our results are fully relevant to the biological situation.

It is important to notice that if the contractile domain is not embedded in an elastic continuum, the equilibrium configuration will not be anisotropic, as may be seen by directly solving Equation (1) analytically. In this simpler case, a solution can be found by assuming that the solution is linear, i.e. $u_x = b_x x$, $u_y = b_y y$, with $b_{x,y}$ - constants, and using the boundary conditions. Thus, the conclusion that the deformation remains anisotropic at long times appears a consequence of the particular geometry in our problem. Note that the main effect described in our model is a special case of a more general

phenomenon when an (elastic) solid body is subjected to uniform isotropic active stress: when mechanical equilibrium sets in, total stress needs not remain either isotropic or uniform. A further discussion of a similar effect in the context of a different developmental model, *C. elegans*, may be found in (Vuong-Brender et al. 2017). Also, related effects for the case of a viscous model were previously discussed in (Salbreux et al. 2009).

3.3 Analysis of the model: laser ablations

Next, we tested whether the model correctly predicts the outcome of laser ablation experiments. Specifically, it has been shown that when the surface of the mesoderm is laser ablated to create an initially round hole, the hole will expand predominantly along the longer axis of the embryo. This anisotropy of the response to ablation appears to increase as gastrulation proceeds: immediately after the onset of gastrulation the response to ablation is approximately isotropic; later ablations become gradually more anisotropic with time (Martin et al. 2010).

To simulate these experiments, we implement the model with a rectangular contractile domain as before, but after the deformation field is evolved to mechanical equilibrium edges within a circular region to mimic a laser ablation, Figure 3a. The initially round hole expands anisotropically, with its long axis aligned with the long axis of the contractile domain. This result qualitatively agrees well with the experiments.

To see this intuitively, let us again consider the model in Figure 2b,c. After the onset of contraction, the domain will shrink more along the shorter vertical direction and less along the perpendicular horizontal direction. Now, consider what would happen if one were to remove a single vertical spring-edge in the interior of the contractile domain after contraction sets in (Figure 3b). This vertical spring-edge has two adjacent vertical edges, colored blue in Figure 3b. If the contractile domain had already undergone some contraction, those adjacent vertical neighbors would have shrunk to become shorter than their preferred rest length. Spring forces in those adjacent spring edges would tend to expand those adjacent springs, thus counteracting the expansion of the “hole” along the vertical direction. Now, instead, consider what would happen if a horizontal spring-edge is removed. The adjacent horizontal spring-edges (colored green in Figure 3b) are under relatively less compression (i.e. deviate less from their rest length). Thus, elastic forces in those springs will counteract the expansion of the “hole” to a lesser extent than

was the case with the vertical spring-edge. In this argument, it has been assumed that *active* forces on every spring in the interior of the contractile domain are the same on every edge of the network. Note that in order to correctly interpret the outcome of the ablation experiments it is absolutely necessary to distinguish between “total stress”, “elastic stress” and “active stress”. Elastic stress is due to the springs. Active stress is due to the motors (myosin). Total stress is the sum of the two. Ablation experiments measure total stress which becomes increasingly anisotropic in the course of the contraction. Active stress, however, remains isotropic throughout the course of the dynamics. Previously, the anisotropy in response to ablation was interpreted as evidence for anisotropy of the active stress (Martin et al. 2010). The present model provides a significantly simpler interpretation: total stress must become anisotropic if the domain is asymmetric (and if the tissue is elastic), whereas active stress need not be anisotropic. Also, in the present model, the asymmetry of contraction is the cause, not a consequence, of anisotropic total stress as measured by laser ablation.

4 Discussion

This paper introduces a simple model that can explain the asymmetry of contraction of the mesoderm in *Drosophila melanogaster*. In the proposed model, the asymmetry of contraction is a consequence of the asymmetry of the geometry of the contractile domain and not because of e.g. anisotropies in active stresses or graded distribution of those stresses within the contractile domain. Importantly, in our model, anisotropy arises from interactions of the mesoderm with the ambient tissue and is not an inherent property of the mesoderm itself. Let us now compare and contrast the proposed mechanism with a number of alternative models.

One alternative possibility is that active stresses in the contractile domain are anisotropic, i.e. the cells have a preferred axis along which to exert active stress. We believe that this scenario is unlikely. First, there is no evidence of planar cell polarity in prospective mesodermal cells of the ventral furrow. Moreover, this interpretation is at odds with the observations by Leptin and Roth (Leptin and Roth 1994), where it was shown that contractile grafts of mesodermal tissue contract along their shorter dimension regardless of their position or orientation within the embryo. If active stresses in those contractile patches were anisotropic, there has to exist a mechanism to align

those active stresses with the shorter axis of the domain through some self-organized process. This general idea has been proposed, but a concrete mechanism has not been demonstrated (Chanet et al. 2017). Although not impossible, this appears a much more complicated explanation than the one we propose. Additionally, if active stresses were anisotropic at the onset of contraction, the anisotropy as measured by laser ablation experiments would be present immediately after the onset of contraction, rather than building up gradually, as has been shown experimentally (Martin et al. 2010).

A second model could hold that material properties of the contractile domain are anisotropic. For instance, one can imagine that the cells of the contractile domain are easier to contract along the mediolateral axis than along the anteroposterior direction. This possibility may be refuted on the same basis as the possibility of anisotropic active stresses.

Other possible explanations include spatial nonuniformity of active stresses within the contractile domain, or spatial nonuniformity of material properties. For instance, much like in the model proposed in e.g. (Mayer et al. 2010; Behrndt et al. 2012), one could imagine that active stresses are isotropic but form a gradient that peaks at the center of the contractile domain and decays gradually along the mediolateral direction. In this case, it can be shown that contraction would be directed along the mediolateral axis of the embryo (Spahn and Reuter 2013). In fact, there are gradients of gene expression for two regulators of myosin, *t48* and *fog* (Lim et al. 2017), and there may be a gradient of myosin density along the mediolateral axis of the embryo (Lim et al. 2017; Spahn and Reuter 2013), though it is unclear from published data whether the myosin gradient appears early enough to be the cause rather than the consequence of anisotropic constriction. Although these data suggest that graded tension might contribute to anisotropic constriction, this potential mechanism is not sufficient to explain all experimental data. In particular, Leptin and Roth demonstrated (Leptin and Roth 1994) that a patch of transplanted mesodermal cells will consistently constrict along its shorter axis. In these experiments, the patch of transplanted mesodermal cells descended from a small number of transplanted nuclei and it seems highly unlikely that any gradient would be preserved in this process. Therefore, some alternative mechanism must drive anisotropic constriction in this case.

Anisotropy of mesoderm contraction has been the focus of a recent experimental paper (Chanet et al. 2017). There, the authors modified the geometry of the contractile domain by genetic means. The observations ob-

tained in (Chanet et al. 2017) are fully consistent with and complementary to the results from (Leptin and Roth 1994): more symmetric domains constrict less anisotropically. In (Chanet et al. 2017) the anisotropy of constriction was attributed to a mechanosensitive response of mesodermal cells leading to re-orientation of actin filaments perpendicularly to the axis of contraction. Although our work does not rule out this possibility, it shows that such effects are not necessary to explain the key aspects of tissue dynamics.

Crucially, the phenomenology presented in this manuscript may apply widely to other developmental systems. In a number of recent publications (Mayer et al. 2010; Behrndt et al. 2012), the response of embryonic tissue to laser ablation was examined in zebrafish or *C. elegans*. In these studies, the initially round hole generated through ablation expanded asymmetrically to become ellipse-shaped; as mentioned, the same results have been reported in gastrulating *Drosophila* tissue (Martin et al. 2010). In particular, the hole expands more in the direction perpendicular to the axis of tissue contraction. In the former papers, the observation was interpreted as an effect of anisotropic viscous shear (Mayer et al. 2010; Behrndt et al. 2012). In the latter paper, this result was interpreted to mean that actively generated tension was anisotropic (Chanet et al. 2010). In the present manuscript, it is shown that neither anisotropic viscous shear nor anisotropic active tension is required for an anisotropic response to laser ablation. Furthermore, it is shown that an anisotropic response to ablation is an inevitable consequence of tissue elasticity. In this way, the present study provides a simple parsimonious explanation of a series of important observations that we believe may have previously been interpreted incorrectly.

An earlier theoretical work by Spahn et al. (Spahn and Reuter 2013) used a vertex model to study the mechanisms that underlie anisotropic tissue constriction during *Drosophila* gastrulation. Based on this modeling, the authors proposed two potential mechanisms to generate anisotropic constriction. One of these models relied on a gradient of contractility along the dorso-ventral axis; as discussed in the previous paragraph, work from Leptin and Roth (Leptin and Roth 1994) indicates that such a gradient is dispensable for anisotropic constriction. In the second model proposed by Spahn et al. anisotropic constriction could be due to the contractile domain being rigidly anchored at the anterior and posterior domain boundaries (i.e. anisotropy being essentially a boundary effect). This solution seems biologically irrelevant: *Drosophila* mesoderm does not appear to be flanked by a row of cells that are being artificially held fixed at one end. Furthermore,

our model explains anisotropic constriction without invoking such effects.

The model presented here qualitatively agrees with the available experimental data. In the future, this model could be tested more rigorously by systematically mapping the distribution of material properties of the tissue (similar to the approach in (Dobrovinski et al. 2017)) and the distribution of total stress (using e.g. laser ablation). With these data, the pattern of deformation can be determined uniquely without fitting.

Acknowledgement

The authors wish to acknowledge support from the Robert A. Welch Foundation (grant number I-1950-20180324). Also, we wish to thank Miriam Osterfield for helpful discussions.

A Appendix

A.1 Analytical treatment

In this section we solve Equation (1) using Fourier transform. We will be considering Equation (1) on a rectangular domain with side lengths Λ_x and Λ_y . Rectangular contractile region $x_0 < x < L_x - x_0$, $y_0 < y < L_y - y_0$ is assumed to be under constant isotropic active stress of magnitude ϕ . We Fourier-expand $\mathbf{u} = [u_x(x, y), u_y(x, y)]$ as

$$\begin{aligned} u_x &= \sum_{n=0}^{\infty} \sum_{m=0}^{\infty} B_{nm} \sin\left(\frac{\pi n x}{\Lambda_x}\right) \cos\left(\frac{\pi m y}{\Lambda_y}\right) , \\ u_y &= \sum_{n=0}^{\infty} \sum_{m=0}^{\infty} A_{nm} \cos\left(\frac{\pi n x}{\Lambda_x}\right) \sin\left(\frac{\pi m y}{\Lambda_y}\right) . \end{aligned} \tag{A.1}$$

It is useful to introduce simplified notation $\alpha \equiv E/(2(1 + \sigma))$, $\beta \equiv E/(2(1 - \sigma))$. Substituting (A.1) into Equation (1) and collecting coefficients corre-

sponding to the same modes we obtain

$$\begin{cases} -\alpha \left[\left(\frac{\pi n}{\Lambda_x} \right)^2 + \left(\frac{\pi m}{\Lambda_y} \right)^2 \right] - \beta \left(\frac{\pi n}{\Lambda_x} \right)^2 \Big\} B_{nm} - \beta \left(\frac{\pi^2}{\Lambda_x \Lambda_y} \right) nm A_{nm} + \phi_{nm}^b = 0, \\ -\alpha \left[\left(\frac{\pi n}{\Lambda_x} \right)^2 + \left(\frac{\pi m}{\Lambda_y} \right)^2 \right] - \beta \left(\frac{\pi m}{\Lambda_x} \right)^2 \Big\} A_{nm} - \beta \left(\frac{\pi^2}{\Lambda_x \Lambda_y} \right) nm B_{nm} + \phi_{nm}^a = 0, \end{cases} \quad (\text{A.2})$$

where the constant coefficients ϕ_{nm}^b , ϕ_{nm}^a are given by

$$\begin{aligned} \phi_{n0}^b &= \frac{2\phi_0}{\Lambda_x \Lambda_y} \left[\sin \frac{\pi n x_0}{\Lambda_x} - \sin \frac{\pi n (L_x - x_0)}{\Lambda_x} \right] (\Lambda_y - 2y_0) \quad , \\ \phi_{nm}^b &= \frac{4\phi_0}{\Lambda_x \Lambda_y} \left[\sin \frac{\pi n x_0}{\Lambda_x} - \sin \frac{\pi n (\Lambda_x - x_0)}{\Lambda_x} \right] \int_{y_0}^{\Lambda_y - y_0} \cos \frac{\pi m y}{\Lambda_y} dy \quad , \\ \phi_{0m}^a &= \frac{2\phi_0}{\Lambda_x \Lambda_y} \left[\sin \frac{\pi m y_0}{\Lambda_y} - \sin \frac{\pi m (\Lambda_y - y_0)}{\Lambda_y} \right] (\Lambda_x - 2x_0) \quad , \\ \phi_{nm}^a &= \frac{4\phi_0}{\Lambda_x \Lambda_y} \left[\sin \frac{\pi m y_0}{\Lambda_y} - \sin \frac{\pi m (\Lambda_y - y_0)}{\Lambda_y} \right] \int_{x_0}^{\Lambda_x - x_0} \cos \frac{\pi n x}{\Lambda_x} dx \quad . \end{aligned} \quad (\text{A.3})$$

With the obvious identifications, Equations (A.2) have the form

$$\begin{aligned} -\gamma a + \delta b + \phi_a &= 0 \quad , \\ -\gamma b + \delta a + \phi_b &= 0 \quad , \end{aligned} \quad (\text{A.4})$$

which is readily solved as

$$\begin{aligned} a &= \frac{1}{2} \left[\frac{\phi_a + \phi_b}{\gamma - \delta} + \frac{\phi_a - \phi_b}{\gamma + \delta} \right] \quad , \\ b &= \frac{1}{2} \left[\frac{\phi_a + \phi_b}{\gamma - \delta} - \frac{\phi_a - \phi_b}{\gamma + \delta} \right] \quad . \end{aligned} \quad (\text{A.5})$$

Combining Equations (A.1)-(A.5), one obtains an explicit expression for displacement \mathbf{u} as a function of position. Since the complete expression is rather lengthy and not especially telling, we do not give it here. Instead, we present plots showing the solution \mathbf{u} obtained by directly evaluating the (truncated) Fourier-expansion in Figure S1a.

A.2 Numerical Simulations I

The code for all simulations is included as a supplemental file. Simulations in Figure 2 were implemented as follows. We solve boundary problem 1 by introducing an additional term $\partial_t \mathbf{u}$ on the right hand side and evolving the resulting equation to equilibrium. All spatial derivatives were approximated as second order central differences. The displacement of the (outermost) boundary was initially set to zero and not updated (fixed boundary conditions). Since the deformation remained localized away from the boundary throughout the course of the simulation, the particular choice of the boundary conditions is expected to not influence the result. Time integration was done by Euler-forward (explicit) scheme. The domain was discretized into a regular grid of size 800x800; Euler forward step was $dt = 10^{-5}$. In order to avoid development of singularities, we “smeared out” the forces at the boundaries of the contractile domain over a region of finite size. Specifically, force distribution had Gaussian profile $\exp(-r^2/\xi^2)$, with $\xi = 0.3$ (this was however found not to be necessary as no singularities developed in the limit of much smaller ξ). Parameters are listed in the corresponding figure caption.

Figures 2d,e was generated by evaluating the Fourier-expanded expressions given in the next section. The 600 lowest Fourier modes were summed. We checked explicitly that analytical results closely matched the results of the numerical simulations. Note that although our treatment focuses on the description of a flat elastic sheet, it may readily be modified to describe a semi-infinite three-dimensional elastic continuum by replacing the coefficient in front of the last term of Equation 1 with $E/(1 + \sigma)(1 - 2\sigma)$. The major conclusions about the anisotropy of the asymptotic state hold in this case as well.

Simulations in Figure 3 were done using a numerical scheme that differed from simulations in Figure 2 in order to simplify the implementation of ablation. Specifically, instead of using a finite difference scheme, we discretized the domain as an (unstructured) grid of equilateral triangles whose edges are linear springs. It has been shown that this approximation reduces to the equations of linear elasticity (i.e. Equation (1)) in the limit of small strains, see e.g. (Seung and Nelson 1998) and (Liang and Mahadevan 2011). Simulation parameters were chosen as follows. The simulated domain had a size of 2x2, the length of an individual spring edge was 0.03. Stiffness of an individual spring edge was set to 50. The contractile domain had a length of 1.2 and a width of 0.6, and was positioned in the center of the simulated

domain. Edges within the contractile domain were subjected to compressive force of 2.5. We used fixed boundary conditions (as in Figure 2). Ablation was simulated after mechanical equilibrium was reached ($t = 5$) by effectively removing all nodes and edges within a circle of radius 0.025 in the center of the domain. Integration was done using Euler-forward scheme with a time step of $5 \cdot 10^{-4}$.

For the parameter sweep of (1), we non-dimensionalized the equation. Dividing throughout by ϕ_0 , and rescaling length by the width of the contractile domain L_y one obtains the re-scaled equation in the same form as Equation (1), except ϕ_0 set to one, and Young's modulus E replaced by the dimensionless ratio E/ϕ_0 . The non-dimensionalized version of Equation 1 has the following three dimensionless parameters: the ratio of Young's modulus to active stress magnitude E/ϕ_0 , Poisson's ratio σ , and the length to width ratio of the contractile domain L_x/L_y .

The plots in Figures S2c and S3 were constructed using analytical expressions for the solution in terms of Fourier-expansion, see Appendix A.1.

A.3 Numerical Simulations II: Finite Element Implementation

The displacement profiles shown in Figures S2a,b were obtained by solving Equation 1 with the finite element method (FEM) (Zienkiewicz and Taylor, 1991). To that end, we first rewrite Equation 1 in its compact form as:

$$\nabla \cdot \mathbf{s} + \nabla \cdot (\phi \mathbf{I}) = \mathbf{0}, \quad (\text{A.6})$$

where $\phi(x, y)$ is the distribution of the active stress introduced in the main text, \mathbf{I} is the identity tensor and \mathbf{s} is the Cauchy stress tensor in the entire domain. This tensor is related to the displacement field \mathbf{u} through the constitutive relation :

$$\mathbf{s} = \lambda_s (\nabla \cdot \mathbf{u}) \mathbf{I} + 2\mu_s \boldsymbol{\epsilon}(\mathbf{u}), \quad (\text{A.7})$$

where $\boldsymbol{\epsilon}(\mathbf{u}) = \frac{1}{2} (\nabla \mathbf{u} + \nabla \mathbf{u}^T)$ is the strain tensor and λ_s and μ_s are elastic constants which are, in the plane stress approximation, given by:

$$\lambda_s = \frac{E\sigma}{(1+\sigma)(1-\sigma)} \quad , \quad \mu_s = \frac{E}{2(1+\sigma)}.$$

Here, E and σ are, respectively, the Young's modulus and Poisson's ratio introduced in the main text.

A.3.1 Weak formulation

In order to obtain the displacement field using FEM, we use a test function \mathbf{v} and rewrite Equation (A.6) in the following weak form :

$$\int_{\partial\Omega} (\mathbf{s} \cdot \mathbf{n}) \mathbf{v} d(\partial\Omega) - \iint_{\Omega} [\lambda_s (\nabla \cdot \mathbf{u}) (\nabla \cdot \mathbf{v}) + 2\mu_s \boldsymbol{\epsilon}(\mathbf{u}) : \boldsymbol{\epsilon}(\mathbf{v})] d\Omega + \iint_{\Omega} \nabla \phi \cdot \mathbf{v} d\Omega = 0. \quad (\text{A.8})$$

In Equation (A.8), Ω and $\partial\Omega$ are respectively the bulk and boundaries of the numerical domain, while \mathbf{n} is the outward normal vector to $\partial\Omega$.

At this stage, it is straightforward to account for the boundary conditions on the boundaries on the embedding domain. Both in the case of traction-free conditions and zero displacement conditions, the first term of Equation (A.8) vanishes. In the former case, this is easily obtained, since $\mathbf{s} \cdot \mathbf{n} = \mathbf{0}$ on $\partial\Omega$. In the latter case, that term can be reduced to zero by choosing test functions \mathbf{v} that vanish on $\partial\Omega$. Therefore, Equation (A.8) can be simplified as:

$$- \iint_{\Omega} [\lambda_s (\nabla \cdot \mathbf{u}) (\nabla \cdot \mathbf{v}) + 2\mu_s \boldsymbol{\epsilon}(\mathbf{u}) : \boldsymbol{\epsilon}(\mathbf{v})] d\Omega + \iint_{\Omega} \nabla \phi \cdot \mathbf{v} d\Omega = 0. \quad (\text{A.9})$$

Next, we discretize Equation (A.9) by expanding the displacement field in the basis of shape functions (chosen to be the same as the test functions): $\mathbf{u} = \sum_{j=1}^N u_j \mathbf{v}_j$, where the u_j are scalar unknown to be found and N is the number of nodes of the computational domain. Inserting this decomposition into the weak form and letting $\mathbf{v} = \mathbf{v}_i$, the displacement field is obtained by inverting the following linear system:

$$\sum_{j=1}^N A_{ij} u_j = F_i, \quad (\text{A.10})$$

where $A_{ij} = \iint_{\Omega} [\lambda_s \nabla \cdot \mathbf{v}_i \nabla \cdot \mathbf{v}_j + 2\mu_s \boldsymbol{\epsilon}(\mathbf{v}_i) : \boldsymbol{\epsilon}(\mathbf{v}_j)] d\Omega$ are components of the stiffness matrix and $F_i = \iint_{\Omega} \nabla \phi \cdot \mathbf{v}_i d\Omega$ are components of the forcing arising from the active stress.

We discretize the domain Ω with a triangular mesh, choose P2-elements as shape functions and solve the system of equation (A.10) using the finite

element open software FreeFem++ (Hecht, 2012). In building the mesh, we ensure that the contractile (or inner) domain is much more refined than the embedding (or outer) domain. In order to ensure a smooth transition of the mesh between the contractile and embedding parts, we include an intermediate zone where the mesh progresses from being very refined near the inner domain to being lesser refined as one approaches the outer domain. Figure S4 shows the mesh used to obtain the displacement field that we plot on Figure S2b' and Figure S2b'.

A.3.2 Boundary conditions treatment

A.3.2.1 Case of zero displacement condition

In the case of fixed boundary conditions, we use a penalty technique to enforce $u_j = 0$ on the nodes corresponding to the domain boundary. That is, if p is the index of a node located on the boundary, we ascribe to it a very large number and write $A_{pp} = 10^{30}$ as well as $F_p = 0 \times 10^{30}$. Consequently, on the row of the stiffness matrix corresponding to that node, we have $\sum_{j=1}^N A_{pj}u_j \approx 10^{30}u_p = 10^{30} \times 0$, thus leading to $u_p = 0$.

A.3.2.2 Case of zero traction condition

In the case of traction-free boundary conditions, we simply solve Equation (A.10) which was obtained from Equation (A.8) with the traction term $(\mathbf{s} \cdot \mathbf{n})$ put to zero on $\partial\Omega$, the boundary of the embedding domain.

However, unlike in the case of zero displacement conditions on $\partial\Omega$, the embedding domain here is kinematically unconstrained. As a result, we find numerical solutions of Equation (A.10) that contain contributions from rigid modes of the system, i.e. the eigenmodes of the stiffness matrix with zero eigenvalue. Indeed, if \mathbf{u}_s is a solution of Equation (A.10), and if \mathbf{u}_r is an eigenmode of the matrix A_{ij} with zero eigenvalue, then clearly $\mathbf{u}_h = \mathbf{u}_s + \mathbf{u}_r$ is also a solution of Equation (A.10).

In order to compare the displacement field obtained under the conditions of zero displacement to that obtained under the condition of zero traction on $\partial\Omega$, we must first remove the rigid modes contributions from the numerical solution (\mathbf{u}_h). This ensures that both displacement fields correspond to the elastic deformations due the active force only and, in absence of the latter force, the displacement fields would uniformly zero. To that end, we proceed as follow.

We first rewrite the numerical solution in the basis of the eigenmodes \mathbf{m}_j of the stiffness matrix, i.e $\mathbf{u}_h = \sum_{j=1}^N \hat{u}_j \mathbf{m}_j$, where the coefficients of the expansion are given by the dot products $(\mathbf{u}_h \cdot \mathbf{m}_j) = \hat{u}_j$. Then, by identifying the rigid modes as those of the stiffness matrix with zero eigenvalue, we find three such modes (two translations and one rotation) that we note \mathbf{m}_k with $k = 1, 2, 3$. Last, by removing these rigid displacements from the previously computed solution, we obtain the following displacement field due to the active force only:

$$\mathbf{u}_s = \mathbf{u}_h - \sum_{k=1}^3 (\mathbf{u}_h \cdot \mathbf{m}_k) \mathbf{m}_k. \quad (\text{A.11})$$

It is the displacement field \mathbf{u}_s that we show in Figure S2b and Figure S2b'.

References

- [1] **Demerec M.** (1994). *Biology of Drosophila*. Cold Spring Harbor Laboratory Press, ISBN-10: 0028438701, ISBN-13: 978-0028438702.
- [2] **Campos-Ortega J.A., Hartenstein V.** (2013). *The Embryonic Development of Drosophila melanogaster*. Springer Verlag, ISBN13 9783662224915, ISBN10 3662224917.
- [3] **Müller H.-A. J., Wieschaus E.** (1996). *armadillo, bazooka, and Stardust* are Critical for Early Stages in Formation of the zonula adherens and Maintenance of the Polarized Blastoderm Epithelium in *Drosophila*. *J. Cell Biol.* **134**, 1, 149-163.
- [4] **Sweeton D., Parks S., Costa M., Wieschaus E.** (1991). Gastrulation in *Drosophila*: the formation of the ventral furrow and posterior midgut invaginations. *Development.* **112**, 775-789.
- [5] **Leptin M., Grunewald B.** (1990). Cell shape changes during gastrulation in *Drosophila*. *Development.* **110**, 73-84.
- [6] **Dawes-Hoang R.E., Parmar K.M., Christiansen E.A., Phelps C.B., Brand A.H., Wieschaus E.F.** (2005). *folded gastrulation*, cell shape change and the control of myosin localization. *Development.* **132**, 4165-4178.
- [7] **Lepin M.** (1991). *twist* and *snail* as positive and negative regulators during *Drosophila* mesoderm development. *Genes Dev.* **5**, 1568-1576.
- [8] **Martin A., Kaschube M., Wieschaus E.** (2009). Pulsed contractions of an actin-myosin network drive apical constriction. *Nature.* **457**, 495-499.
- [9] **M. Leptin and S. Roth.** (1994). Autonomy and non-autonomy in *Drosophila* mesoderm determination and morphogenesis. *Development.* **120**, 853-859.
- [10] **Salbreux G., Prost J., and Joanny J.F.** (2009) Hydrodynamics of Cellular Cortical Flows and the Formation of Contractile Rings. *Phys. Rev. Lett.* **103**, 058102.
- [11] **Martin A.C., Gelbart M., Fernandez-Gonzalez R., Kaschube M., Wieschaus E.** (2010). Integration of contractile forces during tissue invagination. *J. Cell Biol.* **188**, 735.
- [12] **Dobrovinski K., Swan M., Polyakov O., Wieschaus E.** (2017). Measurement of cortical elasticity in *Drosophila melanogaster* embryos using ferrofluids. *PNAS.* **114**, 5, 1051-1056.
- [13] **Landau L.D., Lifshitz E.M.** (1970). *Theory of Elasticity (Volume 7 of A Course of Theoretical Physics)*. Pergamon Press.

- [14] **Jülicher F., Kruse K., Prost J., Joanny J.-F.** (2007). Active behavior of the cytoskeleton. *Phys. Rep.* **449**, 3-28.
- [15] **Greaves G.N., Greer A.L., Lakes R.S., Rouxel T.** (2011) Poisson's ratio and modern materials. *Nat. Mater.* **10**, 823-837.
- [16] **Vuong-Brender T.T.K., Amar B.A., Pontabry J., Labouesse M.** (2017). The interplay of stiffness and force anisotropies drive embryo elongation. *6*, eLife, e23866.
- [17] **Mayer M., Depken M., Bois J.S., Jülicher F., Grill S.W.** (2010) Anisotropies in cortical tension reveal the physical basis of polarizing cortical flows. *Science* **467**, 617-621.
- [18] **Behrndt M., Salbreux G., Campinho P., Hauschild R., Oswald F., Roensch J., Grill S.W., Heisenberg C.-P.** (2012). Forces driving epithelial spreading in zebrafish gastrulation. *Science* **338**, 257.
- [19] **Chanet S., Miller J. C., Vaishnav E. D., Ermentrout B., Davidson L. A., Adam Martin A. C.** (2017). Actomyosin meshwork mechanosensing enables tissue shape to orient cell force. *Nature*. **8**, 15014.
- [20] **Spahn P., Reuter R.** (2013). A vertex model of *Drosophila* ventral furrow formation. *PLoS ONE* **8**, 9, e75051.
- [21] **Lim B., Levine M., Yamazaki Y.** Transcriptional pre-patterning of *Drosophila* gastrulation. (2017). *Curr. Biol.* **27**, 3, 286-290.
- [22] **Guglielmi G., Barry J.D., Huber W., De Renzis S.** An Optogenetic Method to Modulate Cell Contractility during Tissue Morphogenesis. *Developmental Cell.* **35**, 5, 646-660.
- [23] **Seung H.S., Nelson D.R.** (1988). Defects in flexible membranes with crystalline order. *Phys. Rev. A.* **38**, 1005.
- [24] **Liang H., Mahadevan L.** (2011). Growth, geometry, and mechanics of a blooming lily. *PNAS.* **108**, 5516-5521.
- [25] **O. C. Zienkiewicz and R. L. Taylor.** (1991). *The Finite Element Method.* McGraw-Hill.
- [26] **F. Hecht.** (2012). New development in freefem++. *J. Num. Math.*, **20**, 251.

Figures

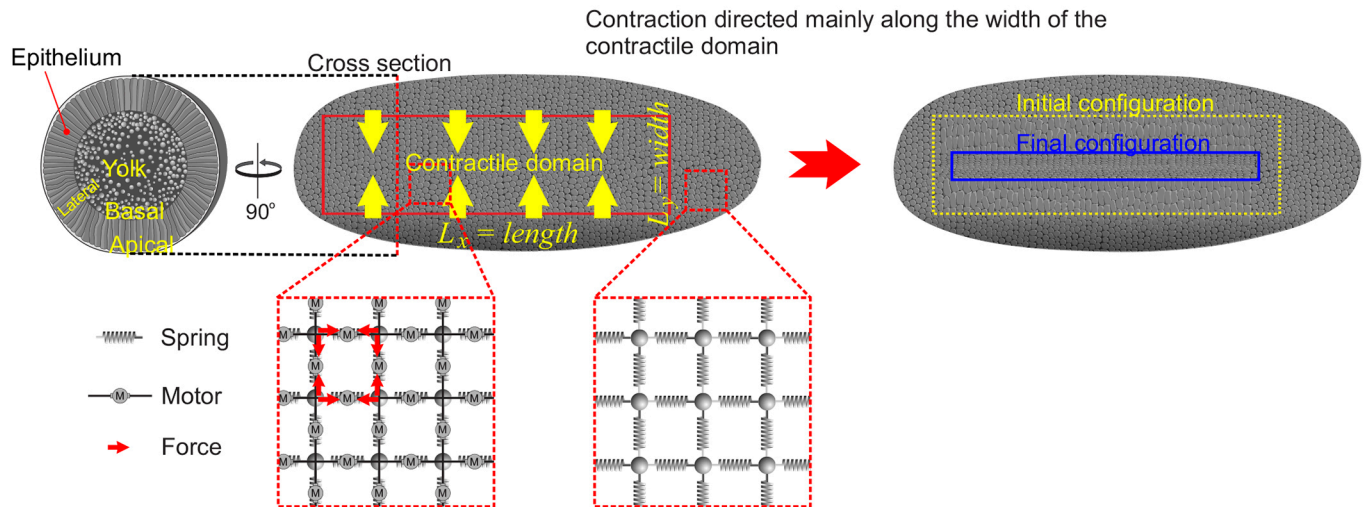


Figure 1

Model for gastrulation. Upper panel: schematic of tissue dynamics. Lower panels: illustration of the model. Left: Cross section through *Drosophila* embryo. The embryo consists of a single layer of epithelial cells surrounding a central unstructured yolk sack. Apical surfaces face outward, basal surfaces face inward. Middle: the contractile domain (mesoderm) is comprised of a rectangular patch of cells some 20 cells wide and 80 cells long. Elastic elements are illustrated as springs and active forces are represented by “motors” (circles with letter “M”). Both are attached to the two adjacent “beads” in parallel. Beads are assumed to feel viscous drag from the ambient environment when moving. Note that it is assumed that forces exerted by motors are constant in time and space. Right: contractile region shrinks anisotropically, contracting much stronger along the width than along the length.

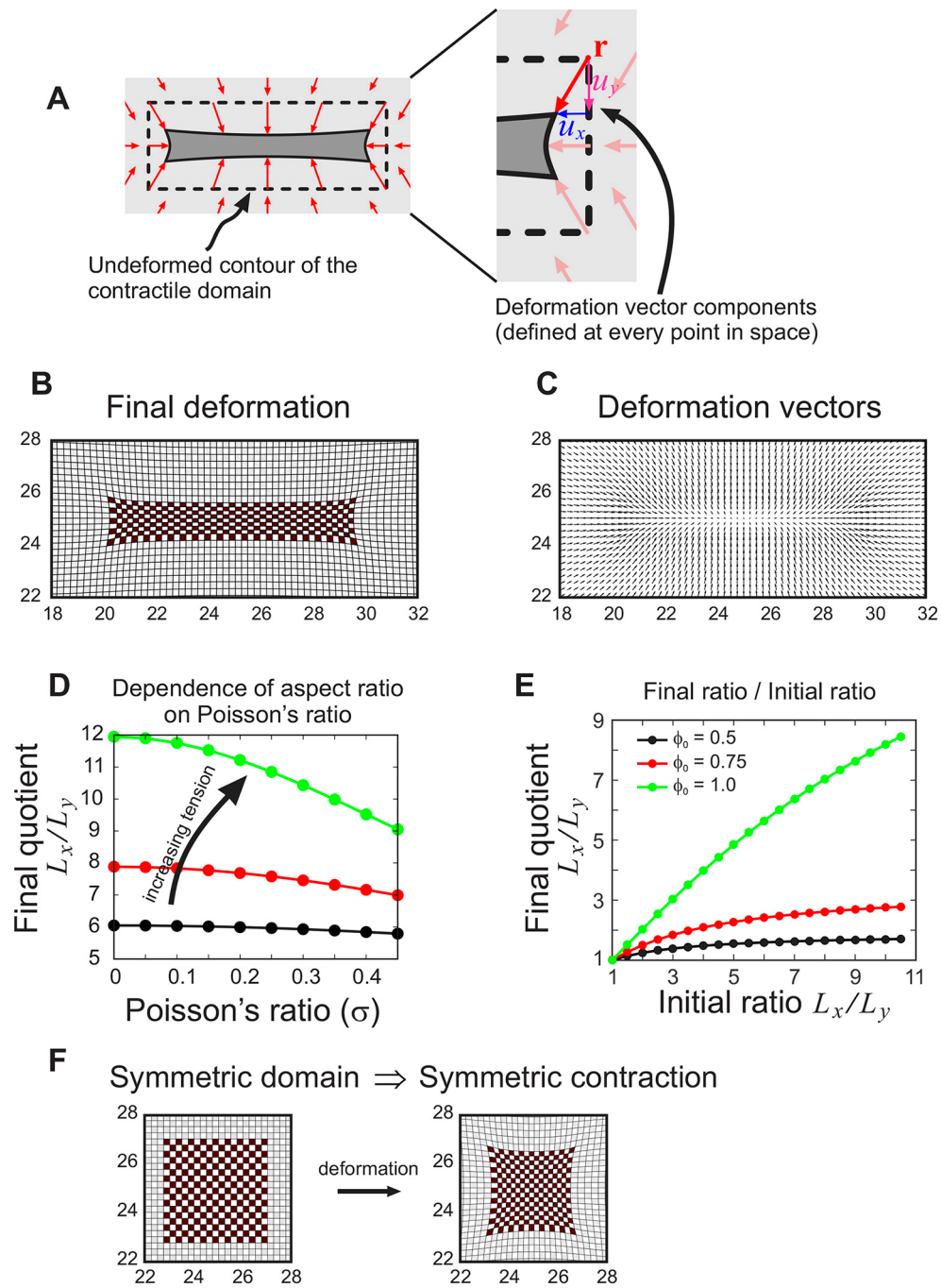


Figure 2

Simulations of the model. a). Schematic showing the geometry of the problem and the quantities describing the resulting deformation. After the deformation sets in, a point located at spatial position \mathbf{r} displaces to a new spatial position $\mathbf{r} + \mathbf{u}(\mathbf{r})$, where \mathbf{u} has components u_x and u_y . b). An example of a final mechanical equilibrium state. Parameters are: $E = 1$, $\sigma = 0.2$, $\phi_0 = 0.5$, (see main text for notation), entire domain size is 50×50 , contractile domain is 10×2 . For readability only the noticeably deformed middle portion of the domain is shown. Simulation was done using finite differences. c). Same simulation as b) showing the distribution of the deformation as a field of displacement vectors. d). Asymptotic (equilibrium) aspect ratio of the contractile domain as a function of Poisson's ratio (x -axis) and contractile active stress (three different curves). All parameters (except the ones that are varied) are as in b,c). Black, red, and green curves correspond to $\phi_0 = 0.5$, $\phi_0 = 0.75$, and $\phi_0 = 1$ respectively. e). Equilibrium length to width ratio (L_x/L_y) of the contractile domain as a function of the initial ratio at time zero for three values of active contractile stress. All parameters except those being varried are as in b). f). Symmetric domains contract isotropically. All parameters except domain size are as in b). Contractile domain size is 4×4 .

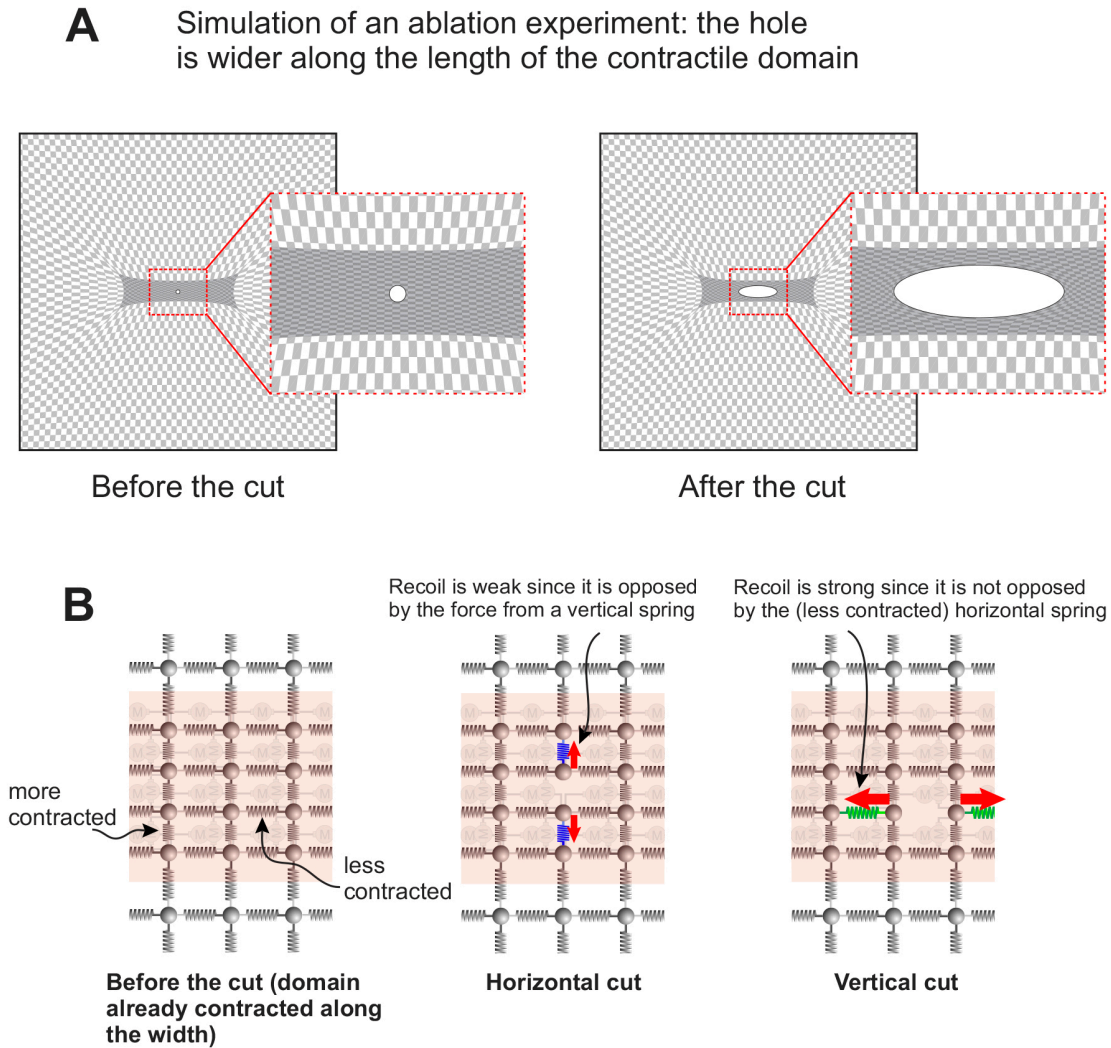


Figure 3

Simulation of an ablation experiment. a). Final state following a simulated laser ablation. A set of vertices in the center of the contractile domain are removed (“ablated”) after a finite deformation sets in. Parameters and the details of implementation are given in Appendix. b). Schematic intuitively explaining the outcome of the simulation in a), see main text for the details.

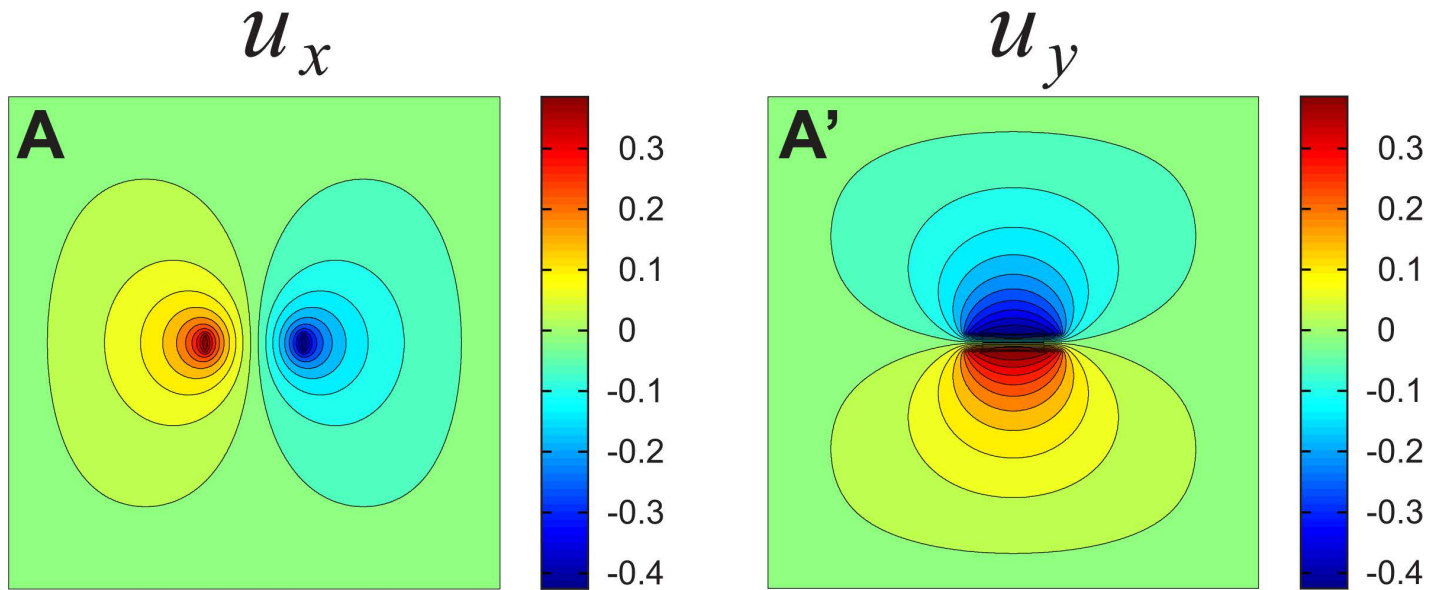
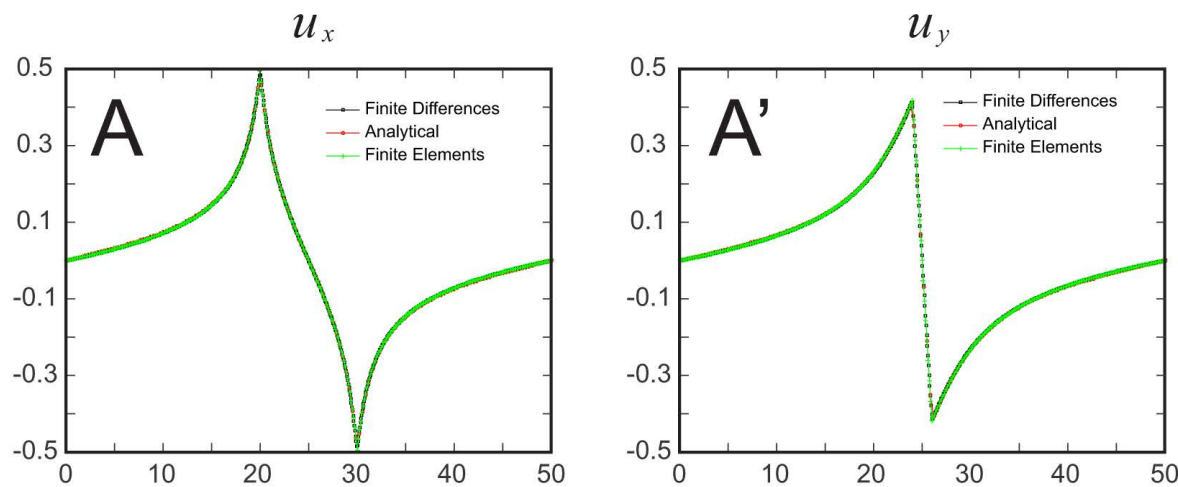


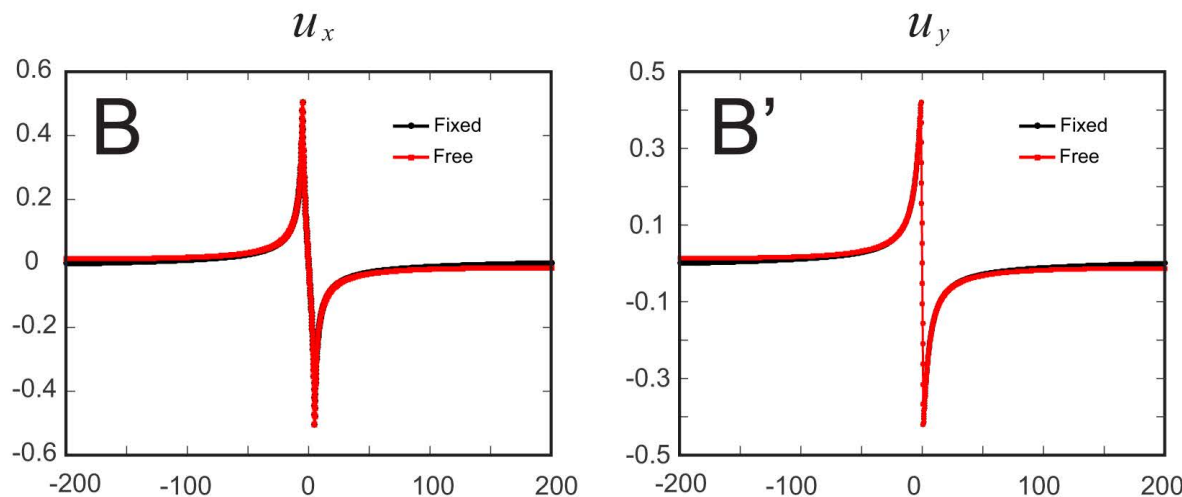
Figure S1

Color plots showing the magnitude of deformation calculated in Figures 2b,c. a). The x-component of the deformation field (u_x) is shown with red colors (positive values) indicating rightwards displacement, and blue colors (negative values) indicating leftwards displacement. b). The y-component of the deformation field u_y ; red (positive) indicates upwards displacement, blue (negative) indicates downwards displacement.

Numerics vs analytics



Fixed vs free boundaries (using finite elements)



Square vs rectangular embedding (from analytical expressions)

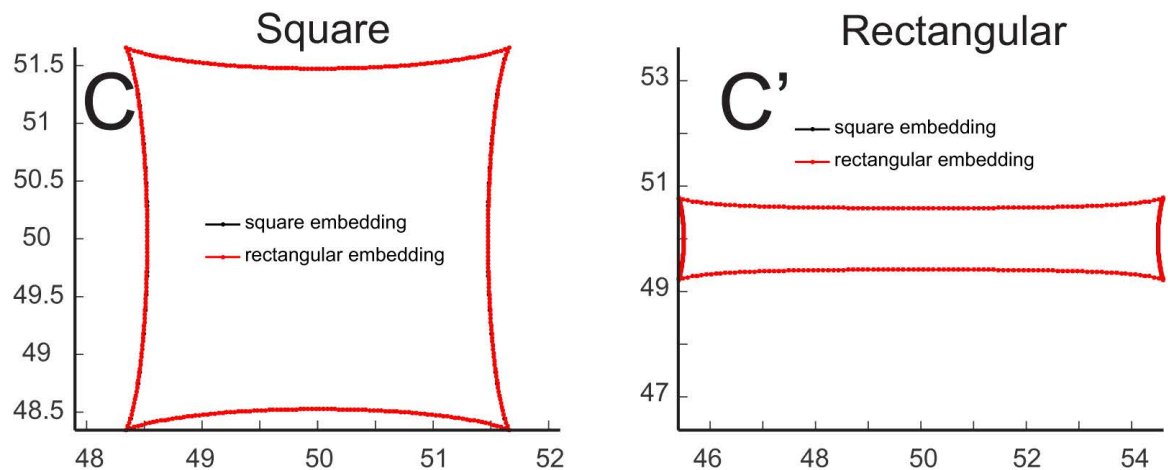


Figure S2

Convergence of solution with respect to the boundary conditions. a). Validation of the numerical scheme. x- and y-components of the displacement field (u_x and u_y) along the vertical and the horizontal cross sections of the simulated domain (at equilibrium). Three curves compare results using two numerical schemes (finite differences and finite elements) and the analytical results using Fourier expansion. Parameters are as in Figure 2b. b). x- and y-components of the displacement field for the case of fixed (black) and free (red) boundary conditions obtained using finite elements. Note particularly close agreement in the vicinity of the contractile domain. All parameters except domain size as in Figure 2b. c). Final shapes of square and rectangular contractile domains embedded in either square or rectangular stress-free domains. The dimensions of the embedding domains were taken to be either 100x100 or 200x100. Initial size of the contractile domain is either 4x4 (left) or 10x2 (right). The two curves essentially coincide, indicating that the geometry of the contractile domain is essentially independent of the boundary conditions (for the chosen domain sizes).

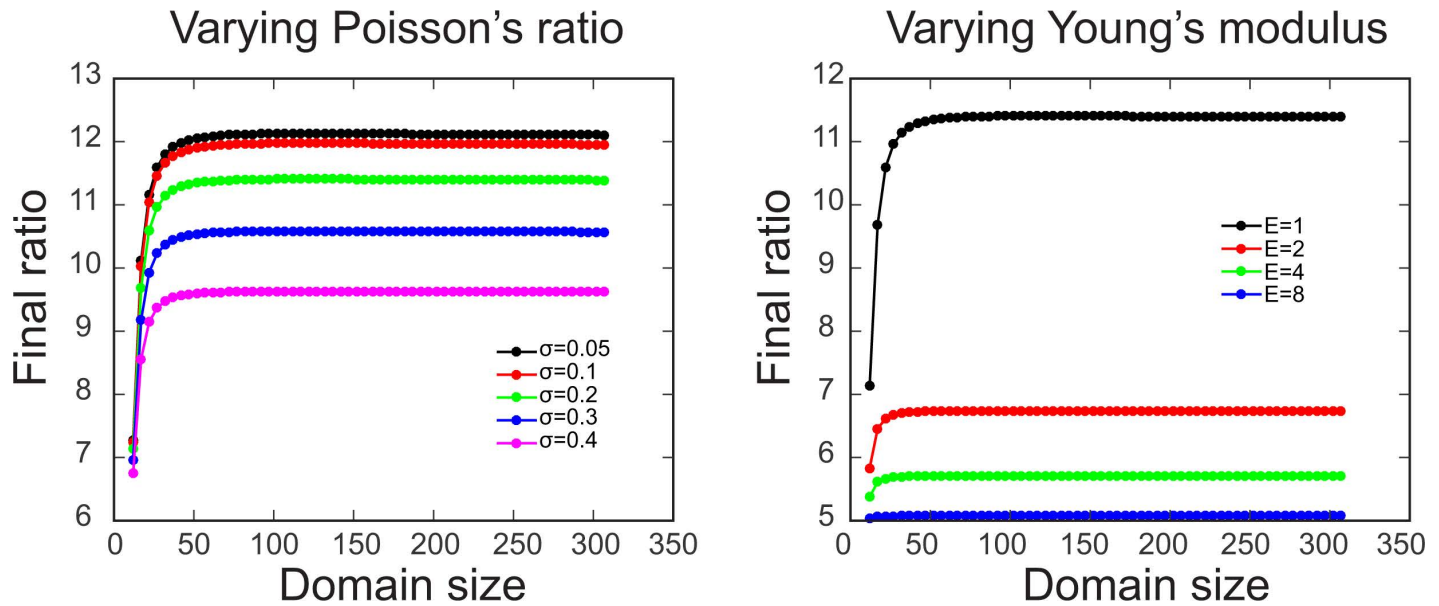


Figure S3

Convergence of the aspect ratio of the contractile domain in the limit of large embedding domain (plotted using analytical expressions). Left: Equilibrium aspect ratio as a function of embedding domain size and Poisson's ratio. Right: Equilibrium aspect ratio as a function of embedding domain size and Young's modulus. For both plots, the length of the embedding domain is labeled on the x-axis; its width is smaller by 8 units (the difference between the length and the width of the contractile domain). The curves were plotted using the Fourier-expansion given in the appendix. Parameters are as in Figure 2b.

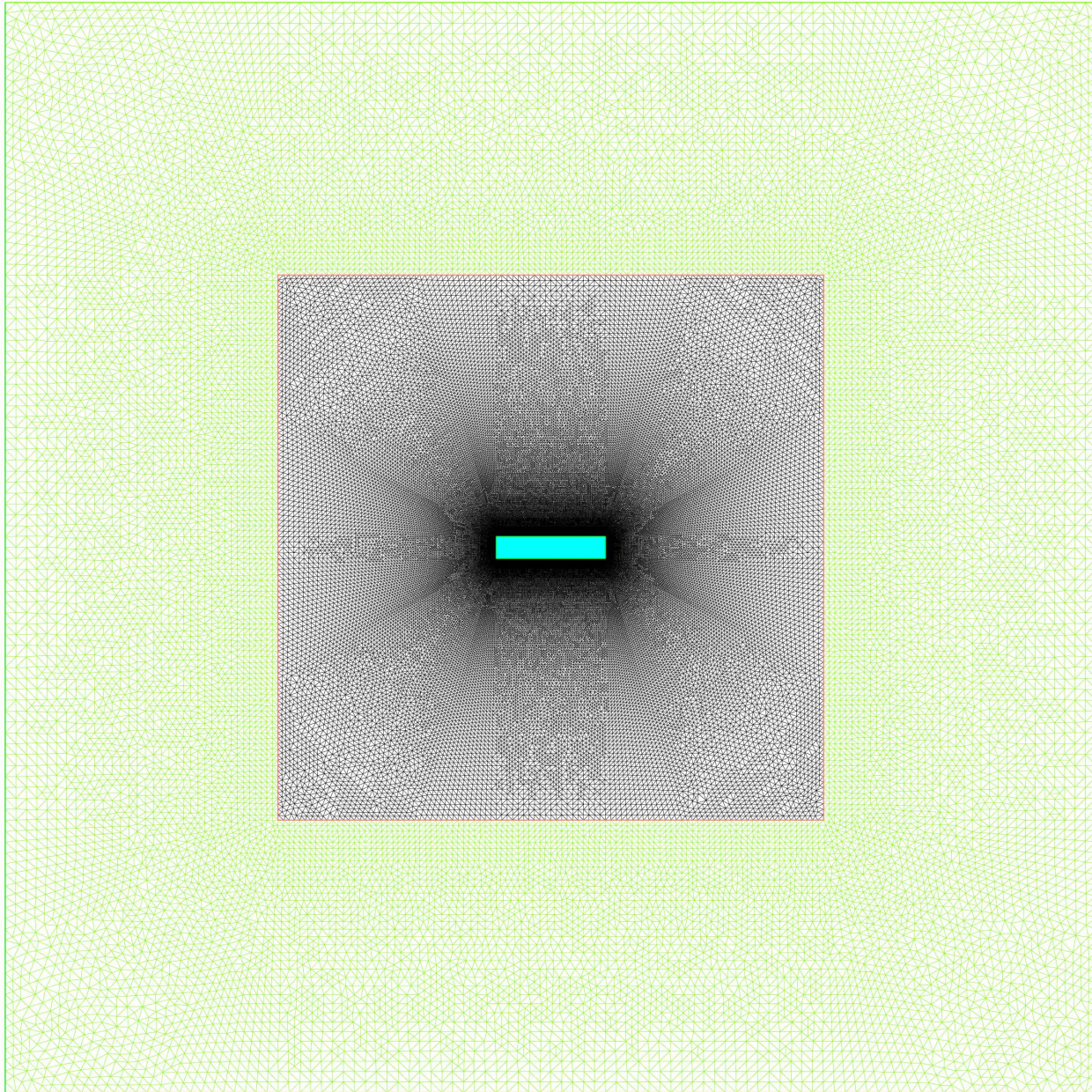


Figure S4

Finite element mesh used for calculation in Figure S2b.

Supplemental code

The content of the zip file with supplemental code is as follows:

`./finite_differences/cont_elast.cpp` C++ source file for finite difference simulation of an elastic shell harboring a rectangular contractile domain.

`./analytics/el_anal_xy_LxLy_comments.mws` Maple file for deriving Fourier coefficients from model parameters.

`./analytics/el_anal.cpp` C++ source file that uses the Fourier coefficients which can be found from `./analytics/el_anal_xy_LxLy_comments.mws` to construct the deformation field by summing the Fourier series.

`./finite_elements/ScriptFreeFem_LameFixedFree.edp` A script to be used with FreeFem++ for simulating an elastic shell harboring a rectangular contractile domain using finite element analysis.

`./ablation/string_tri.cpp` A C++ source file to simulate ablation experiments.

Must be compiled together with `./ablation/outpt.h`. The `./ablation/meshfiles` folder contains files serving input (initial conditions) for this simulation.

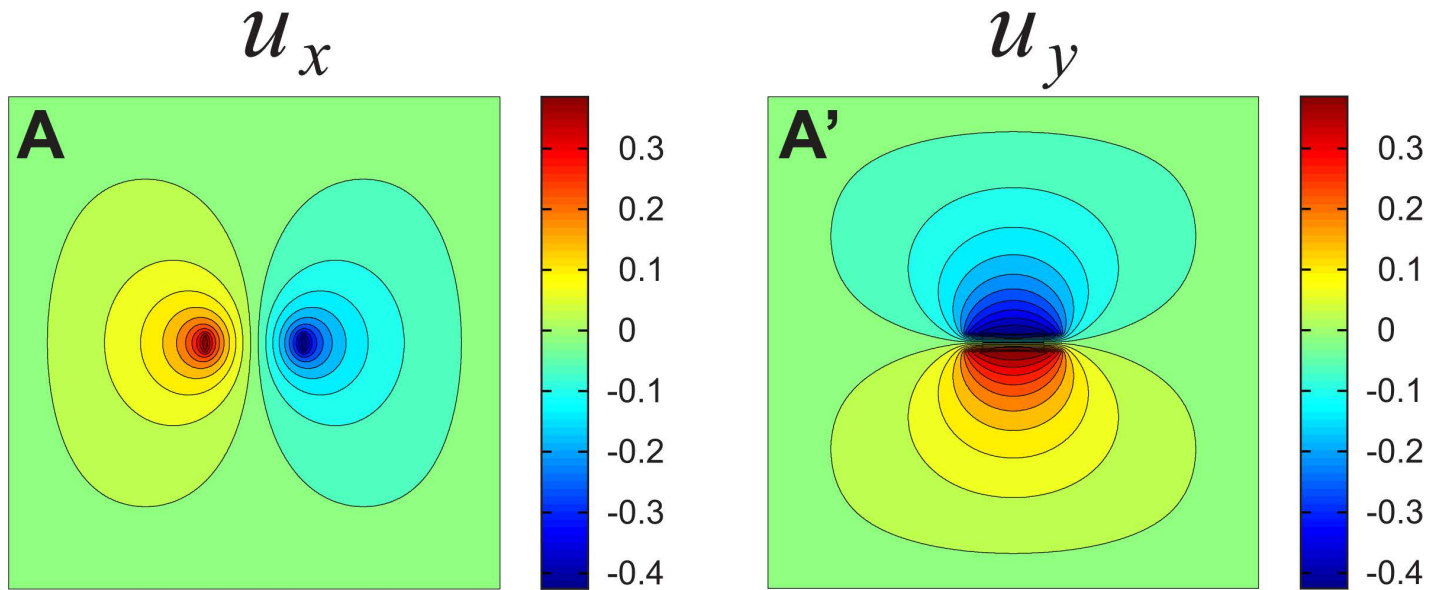
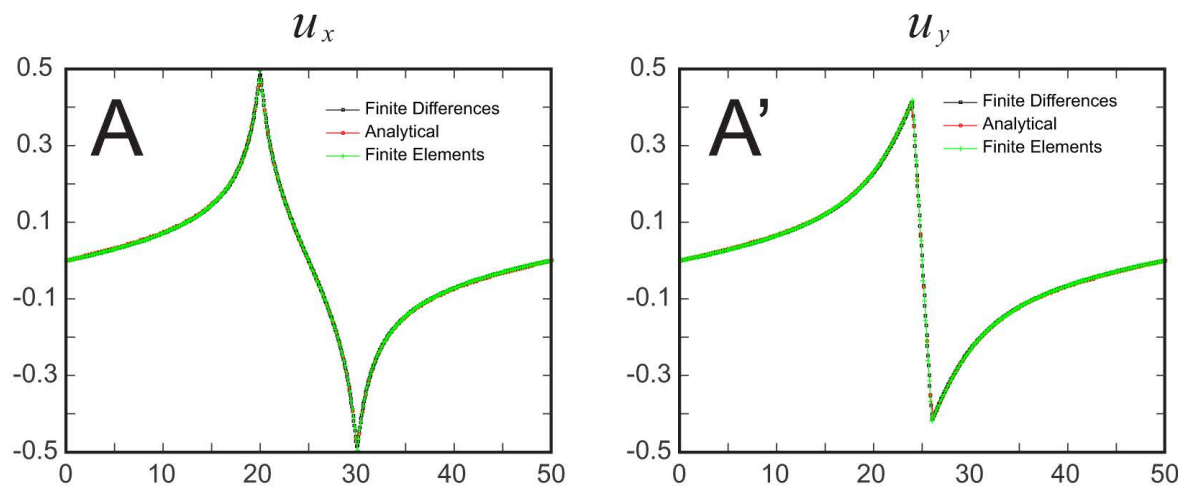


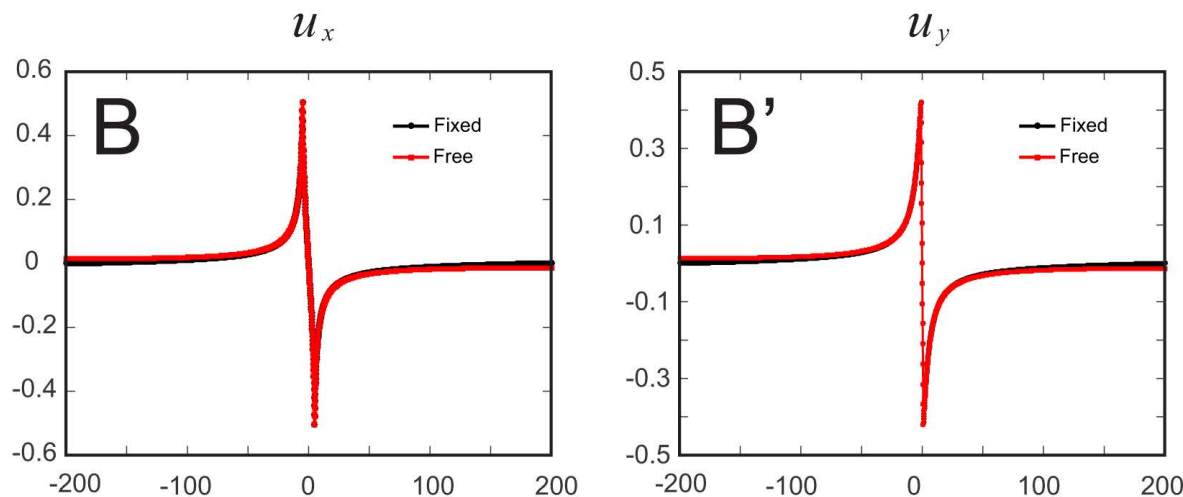
Figure S1

Color plots showing the magnitude of deformation calculated in Figures 2b,c. a). The x-component of the deformation field (u_x) is shown with red colors (positive values) indicating rightwards displacement, and blue colors (negative values) indicating leftwards displacement. b). The y-component of the deformation field u_y ; red (positive) indicates upwards displacement, blue (negative) indicates downwards displacement.

Numerics vs analytics



Fixed vs free boundaries (using finite elements)



Square vs rectangular embedding (from analytical expressions)

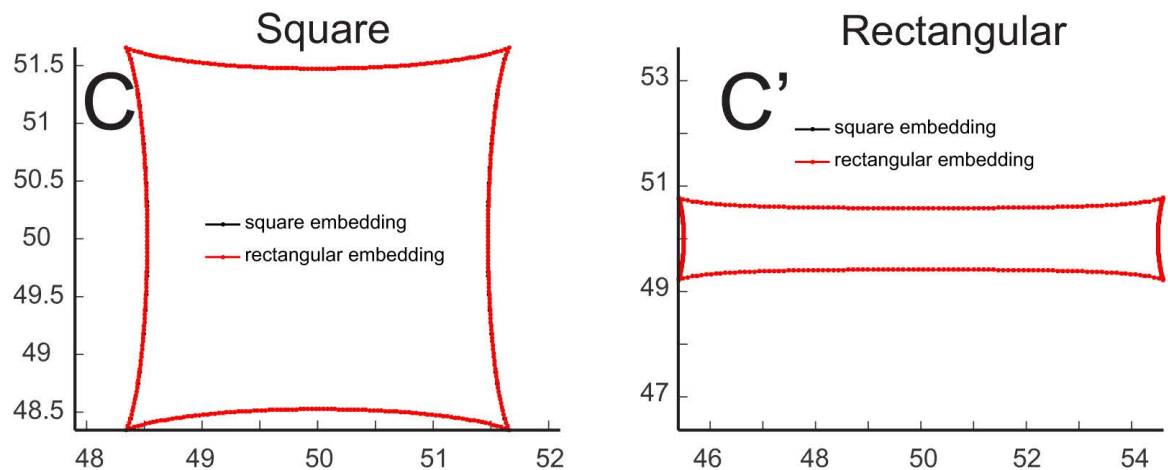


Figure S2

Convergence of solution with respect to the boundary conditions. a). Validation of the numerical scheme. x- and y-components of the displacement field (u_x and u_y) along the vertical and the horizontal cross sections of the simulated domain (at equilibrium). Three curves compare results using two numerical schemes (finite differences and finite elements) and the analytical results using Fourier expansion. Parameters are as in Figure 2b. b). x- and y-components of the displacement field for the case of fixed (black) and free (red) boundary conditions obtained using finite elements. Note particularly close agreement in the vicinity of the contractile domain. All parameters except domain size as in Figure 2b. c). Final shapes of square and rectangular contractile domains embedded in either square or rectangular stress-free domains. The dimensions of the embedding domains were taken to be either 100x100 or 200x100. Initial size of the contractile domain is either 4x4 (left) or 10x2 (right). The two curves essentially coincide, indicating that the geometry of the contractile domain is essentially independent of the boundary conditions (for the chosen domain sizes).

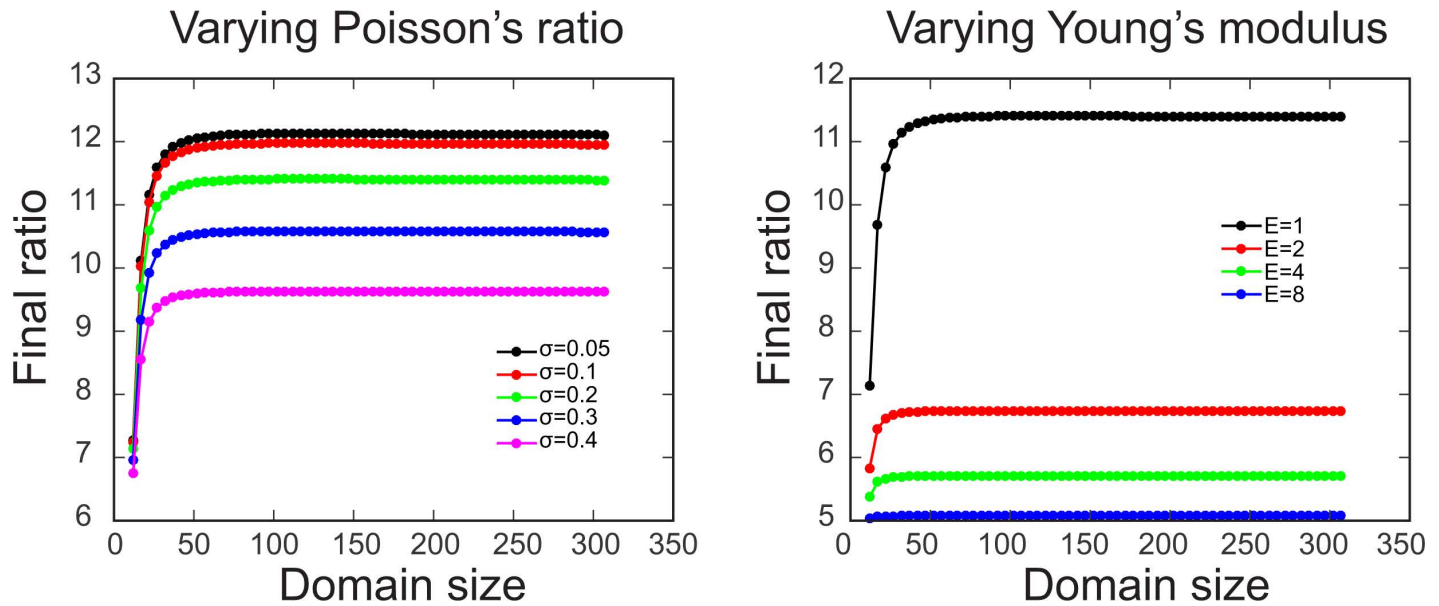


Figure S3

Convergence of the aspect ratio of the contractile domain in the limit of large embedding domain (plotted using analytical expressions). Left: Equilibrium aspect ratio as a function of embedding domain size and Poisson's ratio. Right: Equilibrium aspect ratio as a function of embedding domain size and Young's modulus. For both plots, the length of the embedding domain is labeled on the x-axis; its width is smaller by 8 units (the difference between the length and the width of the contractile domain). The curves were plotted using the Fourier-expansion given in the appendix. Parameters are as in Figure 2b.

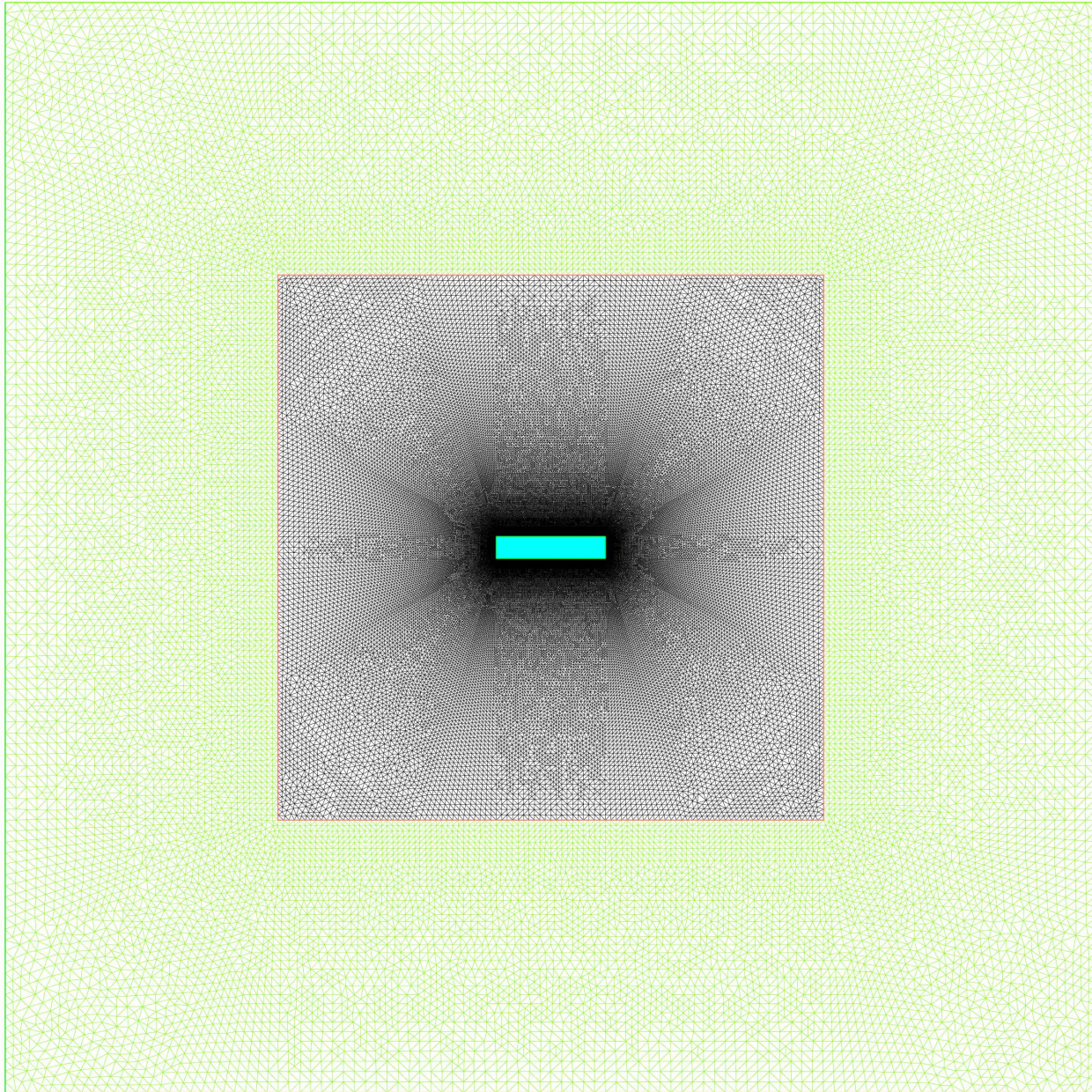


Figure S4

Finite element mesh used for calculation in Figure S2b.

[Click here to Download Supplemental code files](#)